www.sciencemag.org/cgi/content/full/science.1236034/DC1

Supplementary Materials for

Ultrafast Three-Dimensional Imaging of Lattice Dynamics in Individual Gold Nanocrystals

J. N. Clark,* L. Beitra, G. Xiong, A. Higginbotham, D. M. Fritz, H. T. Lemke, D. Zhu, M. Chollet, G. J. Williams, M. Messerschmidt, B. Abbey, R. J. Harder, A. M. Korsunsky, J. S. Wark, I. K. Robinson

*Corresponding author. E-mail: jesse.clark@ucl.ac.uk

Published 23 May 2013 on *Science* Express
DOI: 10.1126/science.1236034

This PDF file includes:

Other Supplementary Material for this manuscript includes the following:
(available at www.sciencemag.org/cgi/content/full/science.1236034/DC1)

Movie S1

Materials and Methods

Sample preparation.

A 2 nm layer of titanium was deposited using thermal evaporation onto an silicon wafer followed by 20 nm of gold. The thin film was then annealed in air at 1000°C for approximately 10 hours after which time the film had dewetted and formed nanocrystals. The nanocrystals cover the substrate uniformly with separations of approximately 1-2 μm between adjacent nanocrystals.

Experiment.

The experiment was performed at the XPP instrument at the LCLS. A 1520×1520 pixel CSPAD with 110 μm square pixels was used to record the diffraction. The Beryllium lenses were positioned so that the sample position was out of the nominal focus. Doing this reduced the incident intensity of the X-ray pulses. This regime was chosen so that the X-ray pulses from the LCLS did not destroy the sample. Damage from either the optical or X-ray pulses was monitored using a confocal microscope (Olympus LEXT) mounted directly above the sample. To record the 3D diffraction pattern, the nanocrystals were rocked in 41 0.02° steps. At each position, 1000 diffraction patterns were recorded. Filtering of the data was done *ex post facto* to remove saturated frames and blank shots, with the final summed patterns consisting of the 100 brightest, non-saturated shots (see Data preparation).

Phase Retrieval

Phase retrieval was performed using a guided approach (*29*). 15 random starts were initiated with each member being subjected to 10 iterations of error reduction (*27*) followed by 160 iterations of hybrid-input output (*27*) and then a further 30 iterations of error reduction. After this first generation, the best iterate was selected and used to generate a further 15 new iterates

(*29*). This process was repeated for a total of 5 generations with the final solution comprising the average of the 5 best iterates. After the phase retrieval was completed, transformation of the image to an orthogonal laboratory frame was performed with the details found elsewhere (*30*). The final resolution was calculated on the transformed image by taking a line-out and fitting a Gaussian to its derivative. The resolution is given as the full-width at half maximum of this Gaussian. This was repeated for each of the orthogonal directions.

Molecular Dynamics Simulations

The simulations were conducted using the LAMMPS package (*31*). The Sheng EAM potential for gold was used (*32*) and was chosen for its accurate recreation of the phonon density of states. A block of material containing 2×10^6 atoms was allowed to thermalise to 300K, having been energy minimised to allow the surfaces to relax. The sample was a cylinder with diameter 44 nm and height 22 nm with the (111) direction along the cylinder axis. After thermalisation, heat was transferred into the system at a decaying exponential rate over 2.5 ps. This approximates the coupling of energy from the electrons (which are formally absent in classical MD, but which will have absorbed the laser light in the experiment) to the ions in a standard two-temperature model. The heat added corresponded to a temperature rise of 270K. The plot in Supplementary Fig. 1 was produced by looking at the Fourier transform along the (11-1) of the atom positions, as a function of time. This effectively follows the movement of the (11-1) peak in reciprocal space. The slices of the cylinder shown in Supplementary Fig. 2 were obtained by calculating the Bragg peak amplitude and phase in the vicinity of the (11-1) Bragg peak. This was then Fourier transformed to obtain a real space representation of the cylinder, entirely analogous to what is recovered in BCDI, where the phase gives the displacement projected onto the scattering vector.

Data preparation

Before phase retrieval can be performed the data needs to be processed to remove detector artefacts and noise. Here we outline the processing used for the preparation of the diffraction patterns before phasing could commence. For each measurement point during the experiment, 1000 XFEL shots were collected. Due to the inherent nature of the processes involved in the XFEL, each shot contains a different number of photons. This fact coupled with the fact that not all shots come in with the same position or incidence angle mean that the number of *diffracted* X-rays from a nanocrystal can vary considerably. As such, screening of the 1000 recorded shots needs to be done. The two screening processes that were employed here were to remove frames that i) had saturated the detector or were close to the limit and ii) remove blank or empty shots which only contribute to the background noise. The detector used was a Cornell-SLAC Pixel Array Detector (*23*) (CS-PAD) which consists of an active area of approximately 1520×1520 110 μm square pixels divided into 32 panels. The CS-PAD was operated in high gain mode where saturation of the pixel occurs at approximately 10000 analogue to digital units (ADU's) with each photon generating approximately 7 ADU's. However non-linearities in the detector response may occur before this limit.Consequently, frames that contain any pixels with values greater than some threshold (3000 ADU's in this case) need to be discarded and do not contribute to the final summed image. After this step was performed the next 100 brightest frames were summed to give the final diffraction pattern. After the 100 brightest frames were selected, a darkfield image was subtracted from the data. The darkfield image consisted of the average of 2000-3000 frames with the XFEL laser off. The darkfield image was subtracted from each frame with a scaling parameter, α, chosen such that the function

$$E = \sum_{n=1}^{N} \left[M(n) \left(\sum_{j=1}^{J} I_j(n) - \alpha \langle I_{DF}(n) \rangle \right)^2 \right] \tag{S1}$$

was minimised. $M(n)$ is a mask applied to select a region where no diffraction was recorded, $I_j(n)$ is the j^{th} frame, $\langle I_{DF}(n)\rangle$ is the average darkfield image, n is the pixel number, N is the total number of pixels and J is the total number of frames. Small departures from unity were found for the values of α which led to a small reduction in residual background noise compared to a value of $\alpha = 1$. Small departures from unity can be attributed to the fluctuations in the number of diffracted photons per XFEL pulse. All diffraction patterns used in the analysis were contained within one of the 32 panels that make up the CS-PAD, therefore no inter-panel calibration was required.

Sensitivity to lattice expansion and contraction in Bragg coherent diffraction imaging

The ability to image projections of the displacement field in Bragg coherent diffraction imaging (BCDI) (*33, 34*) is closely related to geometrical phase analysis (*35, 36*) which is often used in the analysis of transmission electron micrographs. In the case of time resolved BCDI we observe a shift in the Bragg peak which we attribute to uniform expansion/contraction of the lattice (relative to the equilibrium lattice) as well as a non-uniform component. Here we show how the technique is sensitive to both components and that the uniform component can be removed to give the non-uniform component.

We can represent our idealised nanocrystal, $\rho(\boldsymbol{r})$, as the product of an infinite lattice, $l(\boldsymbol{r})$ with a shape function $s(\boldsymbol{r})$ which defines the shape and extent of the nanocrystal via

$$\rho(\boldsymbol{r}) = s(\boldsymbol{r})l(\boldsymbol{r}), \tag{S2}$$

where $\boldsymbol{r}$ is a real-space position vector. Rather than writing the lattice function as a sum of translated delta functions, we can write it as a Fourier series (*35, 36*) via

$$l(\boldsymbol{r}) = \sum_{\boldsymbol{Q}} C_{\boldsymbol{Q}} \exp\left[i\boldsymbol{Q}\cdot\boldsymbol{r}\right] \tag{S3}$$

where $\boldsymbol{Q}$ is a reciprocal lattice vector and $C_{\boldsymbol{Q}}$ the complex coefficients. In the case of a lattice that has some local displacements about each position described by the displacement field, $\boldsymbol{u}(\boldsymbol{r})$, we have $\boldsymbol{r} \rightarrow \boldsymbol{r} + \boldsymbol{u}(\boldsymbol{r})$ and the lattice function becomes

$$l(\boldsymbol{r} + \boldsymbol{u}(\boldsymbol{r})) = \sum_{\boldsymbol{Q}} C'_{\boldsymbol{Q}} \exp\left[i\boldsymbol{Q} \cdot (\boldsymbol{r} + \boldsymbol{u}(\boldsymbol{r}))\right] \tag{S4}$$

$$= \sum_{\boldsymbol{Q}} C'_{\boldsymbol{Q}} \exp\left[i\boldsymbol{Q} \cdot \boldsymbol{u}(\boldsymbol{r})\right] \exp\left[i\boldsymbol{Q} \cdot \boldsymbol{r}\right] \tag{S5}$$

$$= \sum_{\boldsymbol{Q}} G_{\boldsymbol{Q}}(\boldsymbol{r}) \exp\left[i\boldsymbol{Q} \cdot \boldsymbol{r}\right] \tag{S6}$$

where the definition of $G_{\boldsymbol{Q}}(\boldsymbol{r})$ is implied by Eq. S5 and Eq. S6. Now taking the Fourier transform of the distorted lattice in Eq. S6 to get

$$\hat{L}(\boldsymbol{q}) = \int l(\boldsymbol{r} + \boldsymbol{u}(\boldsymbol{r})) \exp\left[-i\boldsymbol{q} \cdot \boldsymbol{r}\right] \mathrm{d}\boldsymbol{r} \tag{S7}$$

$$= \int \sum_{\boldsymbol{Q}} G_{\boldsymbol{Q}}(\boldsymbol{r}) \exp\left[i\boldsymbol{Q} \cdot \boldsymbol{r}\right] \exp\left[-i\boldsymbol{q} \cdot \boldsymbol{r}\right] \mathrm{d}\boldsymbol{r} \tag{S8}$$

$$= \sum_{\boldsymbol{Q}} \int G_{\boldsymbol{Q}}(\boldsymbol{r}) \exp\left[i\boldsymbol{Q} \cdot \boldsymbol{r}\right] \exp\left[-i\boldsymbol{q} \cdot \boldsymbol{r}\right] \mathrm{d}\boldsymbol{r} \tag{S9}$$

$$= \sum_{\boldsymbol{Q}} \hat{G}_{\boldsymbol{Q}}(\boldsymbol{q}) \otimes \delta(\boldsymbol{q} - \boldsymbol{Q}), \tag{S10}$$

which shows how the original lattice is now altered due to a displacement field. In the case of $\boldsymbol{u}(\boldsymbol{r}) = 0$, $G_{\boldsymbol{Q}}(\boldsymbol{r}) = constant$ and Eq. S10 simply becomes a reciprocal lattice of $l(\boldsymbol{r})$ given by a series of translated delta functions.

Under the first Born approximation using quasi-monochromatic, spatially coherent X-rays with the diffraction collected in the far-field, the diffracted wavefield, $\hat{\psi}(\boldsymbol{q})$ is adequately described by the Fourier transform of the real space nanocrystal density. For a nanocrystal with some

associated displacement field, $\boldsymbol{u}(\boldsymbol{r})$, this becomes (omitting constant pre-factors),

$$\hat{\psi}(\boldsymbol{q}) = \int \rho(\boldsymbol{r}) \exp\left[i\boldsymbol{q}\cdot\boldsymbol{r}\right] \mathrm{d}\boldsymbol{r} \tag{S11}$$

$$= \int s(\boldsymbol{r}) l(\boldsymbol{r} + \boldsymbol{u}(\boldsymbol{r})) \exp\left[i\boldsymbol{q}\cdot\boldsymbol{r}\right] \mathrm{d}\boldsymbol{r} \tag{S12}$$

$$= \hat{S}(\boldsymbol{q}) \otimes \hat{L}(\boldsymbol{q}), \tag{S13}$$

and using the result from Eq. S10 we get,

$$\hat{\psi}(\boldsymbol{q}) = \hat{S}(\boldsymbol{q}) \otimes \sum_{\boldsymbol{Q}} \hat{G}_{\boldsymbol{Q}}(\boldsymbol{q}) \otimes \delta(\boldsymbol{q} - \boldsymbol{Q}) \tag{S14}$$

$$= \sum_{\boldsymbol{Q}} \hat{S}(\boldsymbol{q}) \otimes \hat{G}_{\boldsymbol{Q}}(\boldsymbol{q}) \otimes \delta(\boldsymbol{q} - \boldsymbol{Q}). \tag{S15}$$

The recorded intensity is now given by

$$I(\boldsymbol{q}) = |\hat{\psi}(\boldsymbol{q})|^2 \tag{S16}$$

$$= \left| \sum_{\boldsymbol{Q}} \hat{\psi}_{\boldsymbol{Q}}(\boldsymbol{q}) \right|^2 \tag{S17}$$

$$= \left| \sum_{\boldsymbol{Q}} \hat{S}(\boldsymbol{q}) \otimes \hat{G}_{\boldsymbol{Q}}(\boldsymbol{q}) \otimes \delta(\boldsymbol{q} - \boldsymbol{Q}) \right|^2, \tag{S18}$$

which gives the diffracted intensity as being composed of diffraction peaks localised around reciprocal lattice points $\boldsymbol{Q}$, with the shape being influenced by the Fourier transform of the shape function, $\hat{S}(\boldsymbol{q})$, of the nanocrystal and the additional function $\hat{G}_{\boldsymbol{Q}}(\boldsymbol{q})$ due to the displacement field. Since the diffraction pattern is localised around the points $\boldsymbol{Q}$ the cross terms in Eq. S18 are negligible and can be omitted giving

$$I(\boldsymbol{q}) = \sum_{\boldsymbol{Q}} \left| \hat{S}(\boldsymbol{q}) \otimes \hat{G}_{\boldsymbol{Q}}(\boldsymbol{q}) \otimes \delta(\boldsymbol{q} - \boldsymbol{Q}) \right|^2. \tag{S19}$$

During an experiment we are concerned with the diffraction centered around a particular $\boldsymbol{Q}$ so the diffracted intensity in the vicinity of this reciprocal point is given by

$$I_{\boldsymbol{Q}}(\boldsymbol{q}) = \left|\hat{\psi}_{\boldsymbol{Q}}(\boldsymbol{q})\right|^2 \tag{S20}$$

$$= \left|\hat{S}(\boldsymbol{q}) \otimes \hat{G}_{\boldsymbol{Q}}(\boldsymbol{q}) \otimes \delta(\boldsymbol{q} - \boldsymbol{Q})\right|^2. \tag{S21}$$

In the case of the Bragg coherent diffraction imaging experiment we are interested in the real space representation of $\hat{\psi}_{\boldsymbol{Q}}(\boldsymbol{q})$, which is obtained using phase retrieval (*27*) and is given by

$$\rho_{\boldsymbol{Q}}(\boldsymbol{r}) = \int \hat{\psi}_{\boldsymbol{Q}}(\boldsymbol{q}) \exp\left[i\boldsymbol{q}\cdot\boldsymbol{r}\right] \mathrm{d}\boldsymbol{q} \tag{S22}$$

$$= \int \hat{S}(\boldsymbol{q}) \otimes \hat{G}_{\boldsymbol{Q}}(\boldsymbol{q}) \otimes \delta(\boldsymbol{q} - \boldsymbol{Q}) \exp\left[i\boldsymbol{q}\cdot\boldsymbol{r}\right] \mathrm{d}\boldsymbol{q} \tag{S23}$$

$$= s(\boldsymbol{r}) C'_{\boldsymbol{Q}} \exp\left[i\boldsymbol{Q}\cdot\boldsymbol{u}(\boldsymbol{r})\right] \exp\left[i\boldsymbol{Q}\cdot\boldsymbol{r}\right] \tag{S24}$$

$$= |\rho(\boldsymbol{r})| \exp\left[i\phi(\boldsymbol{r})\right] \tag{S25}$$

where $\phi(\boldsymbol{r})$ is the phase of the real space function $\rho_{\boldsymbol{Q}}(\boldsymbol{r})$, and is given by

$$\phi(\boldsymbol{r}) = \phi_{C'} + \boldsymbol{Q}\cdot\boldsymbol{u}(\boldsymbol{r}) + \boldsymbol{Q}\cdot\boldsymbol{r} \tag{S26}$$

where $\phi_{C'}$ is a constant, $\boldsymbol{Q}\cdot\boldsymbol{r}$ is a phase ramp introduced from selecting a particular $\boldsymbol{Q}$, and $\boldsymbol{Q}\cdot\boldsymbol{u}(\boldsymbol{r})$ is a projection of the displacement field. Since we are interested in relative displacements the constant in the phase term can be removed by setting the average phase to zero (or any other value), additionally the phase retrieval process employed to invert the diffraction patterns in insensitive to phase offsets (*27*). The ramp can also be removed by either direct subtraction or judicious recentering of $\hat{\psi}_{\boldsymbol{Q}}(\boldsymbol{q})$, leaving only the projected displacement. For a homogenous expansion or contraction of the lattice, as is observed in the propagation of acoustic phonons in a nanocrystal, the projection of the N dimensional displacement field takes the form

$$\boldsymbol{Q}\cdot\boldsymbol{u}(\boldsymbol{r}) = \phi_h(\boldsymbol{r}) \tag{S27}$$

$$= \sum_{i=1}^{N} \alpha_i r_i, \tag{S28}$$

where $\phi_h(\boldsymbol{r})$ represents the homogenous component of the projected displacement field and α_i is a real constant with its sign signifying either expansion (positive) or contraction (negative) relative to the lattice (in the direction of $\boldsymbol{Q}$) for a real space direction r_i. It can be seen that the terms in Eq. S28 result in real space phase ramps which manifests as a peak shift in reciprocal space. If there is some homogenous expansion/contraction with some additional inhomogenous expansion/contraction the projected displacement can be written

$$\boldsymbol{Q} \cdot \boldsymbol{u}(\boldsymbol{r}) = \phi_h(\boldsymbol{r}) + \phi_i(\boldsymbol{r}). \tag{S29}$$

To obtain the inhomogenous component, $\phi_i(\boldsymbol{r})$, the phase ramp due to the homogenous component needs to be removed. In practice any ramps can be removed by centering the data. From the Fourier shift theorem which states,

$$\hat{F}(\boldsymbol{q} - \boldsymbol{a}) = \int f(\boldsymbol{r}) \exp\left[i\boldsymbol{a} \cdot \boldsymbol{r}\right] \exp\left[i\boldsymbol{q} \cdot \boldsymbol{r}\right] \mathrm{d}\mathbf{r} \tag{S30}$$

it can be seen that the recentering of $\hat{F}(\boldsymbol{q} - \boldsymbol{a})$ ($\hat{\psi}_{\boldsymbol{Q}}(\boldsymbol{q})$ in the experiment) removes the ramp in real space.

Removal of phase ramp and image registration

To remove any real space phase ramp in $\rho_{\boldsymbol{Q}}(\boldsymbol{r})$, its Fourier transform, $\hat{\psi}_{\boldsymbol{Q}}(\boldsymbol{q})$, needs to be recentered. The problem now becomes what is the best way to determine the center of $\hat{\psi}_{\boldsymbol{Q}}(\boldsymbol{q})$. For real objects, the center of mass of $|\hat{\psi}_{\boldsymbol{Q}}(\boldsymbol{q})|$ is an appropriate choice to determine the center as the diffraction pattern is centro-symmetric and will have a well defined central maxima. For complex objects that have non-negligible phase, the center of mass may not be appropriate due to the fact $|\hat{\psi}_{\boldsymbol{Q}}(\boldsymbol{r})|$ may contain multiple peaks and be asymmetrical. In the case here, we have found an appropriate method consisted of centering $\hat{\psi}_{\boldsymbol{Q}}(\boldsymbol{r})$ based on the center of mass of $|\hat{\psi}_{\boldsymbol{Q}}(\boldsymbol{r})|^4$. Sub pixel shifting was achieved by multiplying $\rho_{\boldsymbol{Q}}(\boldsymbol{r})$ by the appropriate phase ramp determined from the center of mass. After this procedure was performed the phase of $\rho_{\boldsymbol{Q}}(\boldsymbol{r})$

was equal to the inhomogenous component (by our definition) of the projected displacement field as is shown in Fig. 3 of the main text.

During the phase retrieval process and for post processing it was necessary to align the reconstructed 3D images with respect to one another. To achieve sub-pixel registration, the two arrays were up-sampled by a factor of k (100 in this case) and the cross-correlation calculated using a 3D implementation of the algorithm found elsewhere (*37*). The location of the maximum in the cross-correlation gives the relative shift of the two images.

Elastic waves in a cylinder

For an isotropic medium the invariant equations of motion are given by (*38*)

$$\mu\nabla^2\boldsymbol{u} + (\lambda+\mu)\nabla\nabla\cdot\boldsymbol{u} = \rho\left(\partial^2\boldsymbol{u}/\partial t^2\right), \tag{S31}$$

where $\boldsymbol{u}$ is the vector displacement field (with position dependance omitted for clarity), ρ is the density and λ and μ are Lamé's constants. Lamé's constants given in terms of the longitudinal (v_l) and transverse (v_t) speeds of sound are $\lambda = \rho\left(v_l^2 - 2v_t^2\right)$ and $\mu = \rho v_t^2$. If we consider a cylinder of radius a and height h the general solutions to Eq. S31 in polar coordinates for the displacement can be written as (*38,39*)

$$\begin{aligned} u_r(r,\theta,y,t) &= u_r(r)\cos(n\theta)\cos(\omega t+\xi y) \\ u_\theta(r,\theta,y,t) &= u_\theta(r)\sin(n\theta)\cos(\omega t+\xi y) \\ u_y(r,\theta,y,t) &= u_y(r)\cos(n\theta)\sin(\omega t+\xi y), \end{aligned} \tag{S32}$$

where u_r, u_θ and u_y are the three components, ω is the angular frequency, ξ is the longitudinal wave number ($m2\pi/h$), r is the radial position vector defined in the $x-z$ plane of Fig. 1 in the main text, θ is the polar angle in the $x-z$ plane, y has the same definition as its cartesian counterpart and $u_i(r)$ are radial dependent functions. n and m are integers used to describe the angular and longitudinal wave numbers respectively and are referenced in the main text as

(n, m) when describing a specific mode. We have approximated the radial functions here with a Bessel function of the first kind with argument $(\pi/R)r$, where R is the radius of the cylinder. The quantity we obtain from the phase retrieval of a single Bragg peak is a projection of the displacement field onto $\boldsymbol{Q}$, as such the quantity we want is given by

$$\boldsymbol{u}_n(r, \theta, y, t) \cdot \boldsymbol{Q} = u_{r,n}(r, \theta, y, t)Q_r + u_{\theta,n}(r, \theta, y, t)Q_\theta + u_{y,n}(r, \theta, y, t)Q_y. \tag{S33}$$

$\boldsymbol{Q}$ represented in the cartesian frame of Fig. 1 is given by,

$$\boldsymbol{Q} = (\sin(\delta)\cos(\gamma), \sin(\gamma), \cos(\delta)\cos(\gamma) - 1) \tag{S34}$$

where the angle δ is the angle the detector makes in the $x - z$ plane, γ is the angle the detector makes in the $z - y$ plane and has been scaled such that the incident wave vector has a magnitude of 1. Shown in Fig. 3 of the main text is an approximate $(n, m) = (1, 1)$ mode projected onto $\boldsymbol{Q}$ using Eq. S32 and Eq. S33 approximating our nanocrystal to a short cylinder of radius 200nm and height (h) 200nm.

Fitted peak shift

The fitted time offsets for three of the oscillations are approximately 20 ps with the other offset being 75 ps (see Supplementary Table 1.). The 20 ps delay could be explained by a measurement offset in the delay time. The 75 ps delay seen in the second oscillation of nanocrystal B is possibly explained by coupling between the nanocrystal and the substrate, which is absent in the first nanocrystal and also absent in a molecular dynamics simulation which is shown in Supplementary Fig. 1. Small time delays have been observed previously and attributed to hot electron pressure (*13,40*) providing an additional force on the nuclei. The total stress is made up of a lattice and an electronic contribution with the force provided by the hot electrons comparable to the driving force but decays more rapidly.

Quality factor comparison

The quality factor, the ratio of damping time to oscillation frequency, ($\frac{1}{2}\omega\tau_d$) for the two frequencies from nanocrystal I are 11.7$\pm$10.3 and 35.7$\pm$10.8 and nanocrystal II are 21.8$\pm$9.1 and 7.28$\pm$9.3. These agree well with quality factors from optical pump-probe measurements on single nanoparticles (*15*) which are in the range of 15-30 and considerably better than values from ensembles with X-ray measurements which are typically < 5 (*26*). However the local environment is likely to influence this value, such as the strength of coupling to the substrate or if the particles are suspended in fluid (*14*).

The damping term appearing in Eq. 1 of the main text has a linear dependance on delay time in its exponent which contrasts with a quadratic dependance found elsewhere (*13, 14*). The primary reason is that here single nanocrystals are probed rather than ensembles. It has been shown (*14*) that sample heterogeneity leads to a quadratic damping term in the exponent which can then be used to determine the distribution of sample sizes.

Supplementary Figures

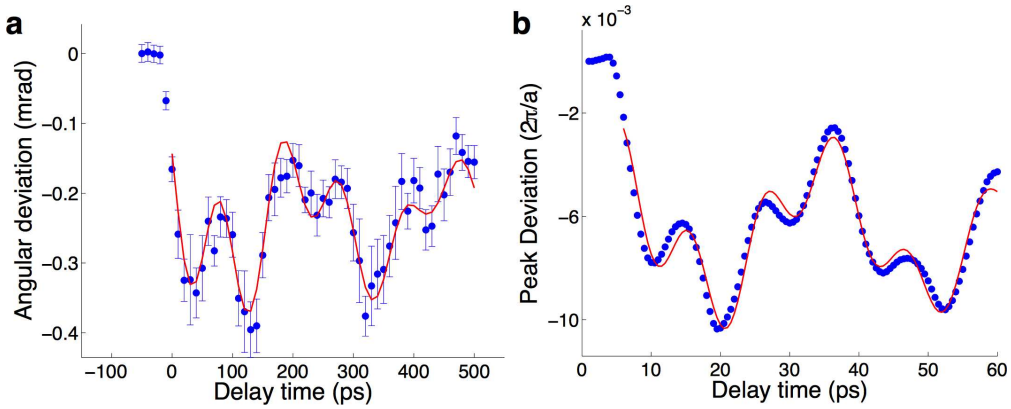

Figure S1: **Comparison of peak shifts from experiment and molecular dynamics simulations**. a, Off-axis (111) peak shift as a function of delay time for nanocrystal I and b, peak shift from a cylinder using a molecular dynamics simulation. Shown in red is the modelled peak shift using two modes. The linear dimensions of the cylinder differ from nanocrystal I by a factor of 9.

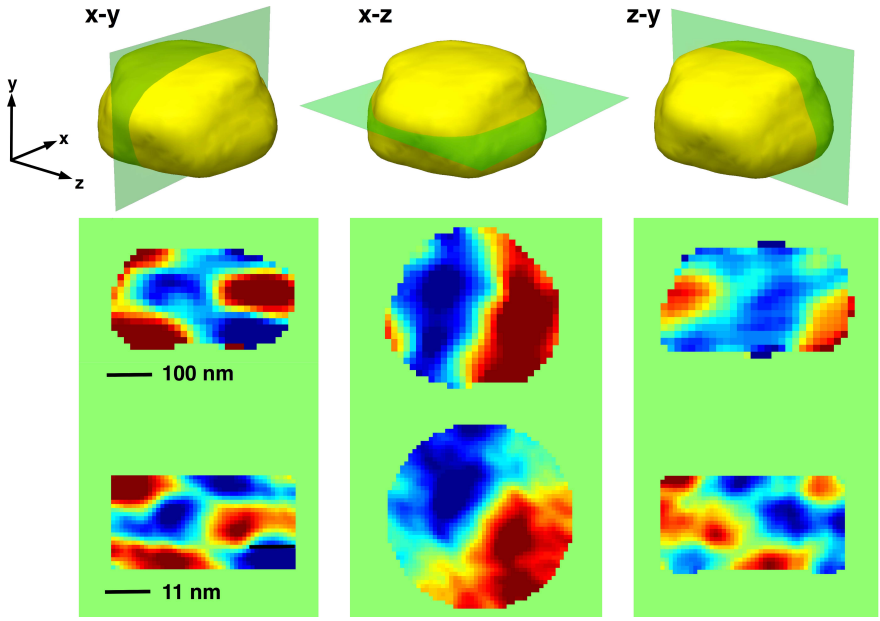

Figure S2: **Comparison of projected displacements from experiment and molecular dynamics simulations**. Orthogonal slices taken either side of the center (top) of nanocrystal I compare the projected displacement obtained from the experiment (middle) to orthogonal slices from a cylinder simulated with molecular dynamics (bottom). The delay time for the experimental data was +110 ps and for the MD simulation was +14 ps. The MD delay time was selected as it is a comparable delay time to the data after taking into account the relative dimensions.

Supplementary Tables

Table S1: **Fitted peak shift parameters** Numerical values obtained from fitting the function $S(\tau) = \sum_{n=1}^{N} A_n \exp\left[-\frac{\tau}{\tau_{d,n}}\right] \cos\left[\frac{2\pi}{T_n}(\tau + \tau_{0,n})\right] + C_n$ to the Bragg peak position shift as a function of delay time. The experimental nanocrystals are denoted as I and II with the MD representing the fitted values for the Molecular Dynamics simulation.

Nanocrystal	Mode (n)	A_n(a.u.)	$\tau_{d,n}$ (ps)	T_n (ps)	$\tau_{0,n}$ (ps)	C_n(a.u.)
I	1	1.3± .37	376 ± 330	101±5	21±4	-0.4
I	2	0.83 ± .31	2742 ± 825	241±11	23±11	-0.4
II	1	1.5±.20	625±261	90±1	20±2	-0.8
II	2	.52±.29	594±762	256±16	75±14	-0.8
MD	1	2.0 ±.32	92±53	10.6±.1	5.8±.44	-2.15
MD	2	2.4 ±.35	4316±270	30.5±.45	-2±.8	-2.15

Movie S1 Movie showing orthogonal slices of the projected displacement for various delay times within the nanocrystal from the reconstructed 3D images.

References and Notes

1. C. Rose-Petruck *et al*., Picosecond-milliangstrom lattice dynamics measured by ultrafast X-ray diffraction. *Nature* **398**, 310–312 (1999). doi:10.1038/18631

2. C. W. Siders *et al*., Detection of nonthermal melting by ultrafast X-ray diffraction. *Science* **286**, 1340–1342 (1999). doi:10.1126/science.286.5443.1340 Medline

3. B. J. Siwick, J. R. Dwyer, R. E. Jordan, R. J. D. Miller, An atomic-level view of melting using femtosecond electron diffraction. *Science* **302**, 1382–1385 (2003). doi:10.1126/science.1090052 Medline

4. K. Sokolowski-Tinten *et al*., Femtosecond X-ray measurement of coherent lattice vibrations near the Lindemann stability limit. *Nature* **422**, 287–289 (2003). doi:10.1038/nature01490 Medline

5. J. Chen, W.-K. Chen, J. Tang, P. M. Rentzepis, Time-resolved structural dynamics of thin metal films heated with femtosecond optical pulses. *Proc. Natl. Acad. Sci. U.S.A.* **108**, 18887–18892 (2011). doi:10.1073/pnas.1115237108 Medline

6. A. M. Lindenberg *et al*., Time-resolved X-Ray diffraction from coherent phonons during a laser-induced phase transition. *Phys. Rev. Lett.* **84**, 111–114 (2000). doi:10.1103/PhysRevLett.84.111 Medline

7. D. M. Fritz *et al*., Ultrafast bond softening in bismuth: Mapping a solid's interatomic potential with X-rays. *Science* **315**, 633–636 (2007). doi:10.1126/science.1135009 Medline

8. R. Ernstorfer *et al*., The formation of warm dense matter: Experimental evidence for electronic bond hardening in gold. *Science* **323**, 1033–1037 (2009). doi:10.1126/science.1162697 Medline

9. A. Cavalleri *et al*., Tracking the motion of charges in a terahertz light field by femtosecond X-ray diffraction. *Nature* **442**, 664–666 (2006). doi:10.1038/nature05041 Medline

10. M. Turner *et al*., Selective oxidation with dioxygen by gold nanoparticle catalysts derived from 55-atom clusters. *Nature* **454**, 981–983 (2008). doi:10.1038/nature07194 Medline

11. S. A. Maier *et al*., Plasmonics—a route to nanoscale optical devices. *Adv. Mater.* **13**, 1501–1505 (2001). doi:10.1002/1521-4095(200110)13:19<1501::AID-ADMA1501>3.0.CO;2-Z

12. M. S. Hanay *et al*., Single-protein nanomechanical mass spectrometry in real time. *Nat. Nanotechnol.* **7**, 602–608 (2012). doi:10.1038/nnano.2012.119 Medline

13. G. V. Hartland, Coherent vibrational motion in metal particles: Determination of the vibrational amplitude and excitation mechanism. *J. Chem. Phys.* **116**, 8048 (2002). doi:10.1063/1.1469021

14. M. Pelton *et al*., Damping of acoustic vibrations in gold nanoparticles. *Nat. Nanotechnol.* **4**, 492–495 (2009). doi:10.1038/nnano.2009.192 Medline

15. M. A. van Dijk, M. Lippitz, M. Orrit, Detection of acoustic oscillations of single gold nanospheres by time-resolved interferometry. *Phys. Rev. Lett.* **95**, 267406 (2005). doi:10.1103/PhysRevLett.95.267406 Medline

16. C.-Y. Ruan, Y. Murooka, R. K. Raman, R. A. Murdick, Dynamics of size-selected gold nanoparticles studied by ultrafast electron nanocrystallography. *Nano Lett.* **7**, 1290–1296 (2007). doi:10.1021/nl070269h Medline

17. A. Plech, V. Kotaidis, S. Grésillon, C. Dahmen, G. von Plessen, Laser-induced heating and melting of gold nanoparticles studied by time-resolved x-ray scattering. *Phys. Rev. B* **70**, 195423 (2004). doi:10.1103/PhysRevB.70.195423

18. P. Emma *et al*., First lasing and operation of an angstrom-wavelength free-electron laser. *Nat. Photonics* **4**, 641–647 (2010). doi:10.1038/nphoton.2010.176

19. J. Miao, P. Charalambous, J. Kirz, D. Sayre, Extending the methodology of X-ray crystallography to allow imaging of micrometre-sized non-crystalline specimens. *Nature* **400**, 342–344 (1999). doi:10.1038/22498

20. M. A. Pfeifer, G. J. Williams, I. A. Vartanyants, R. Harder, I. K. Robinson, Three-dimensional mapping of a deformation field inside a nanocrystal. *Nature* **442**, 63–66 (2006). doi:10.1038/nature04867 Medline

21. Materials, methods are available as supplementary materials on *Science* Online.

22. M. C. Newton, S. J. Leake, R. Harder, I. K. Robinson, Three-dimensional imaging of strain in a single ZnO nanorod. *Nat. Mater.* **9**, 120–124 (2010). doi:10.1038/nmat2607 Medline

23. P. Hart *et al*., The CS-PAD megapixel x-ray camera at LCLS. *Proc. SPIE* **8504**, 85040C–1 (2012). doi:10.1117/12.930924

24. P. B. Allen, Theory of thermal relaxation of electrons in metals. *Phys. Rev. Lett.* **59**, 1460–1463 (1987). doi:10.1103/PhysRevLett.59.1460 Medline

25. G. V. Hartland, M. Hu, J. E. Sader, Softening of the symmetric breathing mode in gold particles by laser-induced heating. *J. Phys. Chem. B* **107**, 7472–7478 (2003). doi:10.1021/jp0276092

26. K. Ichiyanagi *et al*., Laser-induced picosecond lattice oscillations in submicron gold crystals. *Phys. Rev. B* **84**, 024110 (2011). doi:10.1103/PhysRevB.84.024110

27. J. R. Fienup, Phase retrieval algorithms: A comparison. *Appl. Opt.* **21**, 2758–2769 (1982). doi:10.1364/AO.21.002758 Medline

28. A. J. McCulloch *et al*., Arbitrarily shaped high-coherence electron bunches from cold atoms. *Nat. Phys.* **7**, 785–788 (2011). doi:10.1038/nphys2052

29. C.-C. Chen, J. Miao, C. W. Wang, T. K. Lee, Application of optimization technique to noncrystalline x-ray diffraction microscopy: Guided hybrid input-output method. *Phys. Rev. B* **76**, 064113 (2007). doi:10.1103/PhysRevB.76.064113

30. J. N. Clark, X. Huang, R. Harder, I. K. Robinson, High-resolution three-dimensional partially coherent diffraction imaging. *Nat. Commun.* **3**, 993 (2012). doi:10.1038/ncomms1994 Medline

31. S. Plimpton, Fast parallel algorithms for short-range molecular dynamics. *J. Comput. Phys.* **117**, 1–19 (1995). doi:10.1006/jcph.1995.1039

32. H. W. Sheng, M. J. Kramer, A. Cadien, T. Fujita, M. W. Chen, Highly optimized embedded-atom-method potentials for fourteen fcc metals. *Phys. Rev. B* **83**, 134118 (2011). doi:10.1103/PhysRevB.83.134118

33. I. K. Robinson, I. A. Vartanyants, Use of coherent X-ray diffraction to map strain fields in nanocrystals. *Appl. Surf. Sci.* **182**, 186–191 (2001). doi:10.1016/S0169-4332(01)00438-X

34. I. Vartanyants, I. Robinson, Partial coherence effects on the imaging of small crystals using coherent x-ray diffraction. *J. Phys. Condens. Matter* **13**, 10593–10611 (2001). doi:10.1088/0953-8984/13/47/305

35. M. Takeda, J. Suzuki, Crystallographic heterodyne phase detection for highly sensitive lattice-distortion measurements. *J. Opt. Soc. Am. A Opt. Image Sci. Vis.* **13**, 1495 (1996). doi:10.1364/JOSAA.13.001495

36. M. J. Hÿtch, E. Snoeck, R. Kilaas, Quantitative measurement of displacement and strain fields from HREM micrographs. *Ultramicroscopy* **74**, 131–146 (1998). doi:10.1016/S0304-3991(98)00035-7

37. M. Guizar-Sicairos, S. T. Thurman, J. R. Fienup, Efficient subpixel image registration algorithms. *Opt. Lett.* **33**, 156–158 (2008). doi:10.1364/OL.33.000156 Medline

38. D. C. Gazis; Analytical Foundation, Three-dimensional investigation of the propagation of waves in hollow circular cylinders. I. Analytical Foundation. *J. Acoust. Soc. Am.* **31**, 568 (1959). doi:10.1121/1.1907753

39. I. Mirsky, Wave propagation in transversely isotropic circular cylinders Part I: Theory. *J. Acoust. Soc. Am.* **37**, 1016 (1965). doi:10.1121/1.1909508

40. M. Perner *et al*., Observation of hot-electron pressure in the vibration dynamics of metal nanoparticles. *Phys. Rev. Lett.* **85**, 792–795 (2000). doi:10.1103/PhysRevLett.85.792 Medline